EUROPEAN ORGANIZATION FOR NUCLEAR RESEARCH

CERN-EP/80-52
18 April 1980

NUCLEAR SCATTERING RADIOGRAPHY

J.C. Duchazeaubeneix, J.C. Faivre, D. Garretta, B. Guillerminet,

M. Rouger and J. Saudinos

Centre d'Etudes Nucléaires, Saclay, France

P. Palmieri, C. Raybaud and G. Salamon

Centre hospitalier universitaire La Timone, Marseille, France, and

Laboratoire de neuroradiologie et d'exploration cérébrale, Marseille, France

G. Charpak, G. Melchart, Y. Perrin, J.C. Santiard and F. Sauli

CERN, Geneva, Switzerland

ABSTRACT

The quasi-elastic scattering of 1 GeV protons permits the three-dimensional reconstruction of the density distribution in extended bodies. Fast multiwire proportional chambers are used to localize the position of every incoming and outgoing charged particle and determine the coordinates at the interaction vertex. This article describes tests on a human head fixed in Formalin. The confrontation with CT scans and anatomical sections is encouraging. Slices with a volume element of 5.5 mm^3 illustrate the sensitivity of the method. The results display also the ability of the method to select the density distribution of hydrogen by making use of the kinematical relations specific to elastic scattering. Prospects for experimentation with living humans are discussed.

(Submitted to J. Comput. Assist. Tomogr.)

INTRODUCTION

In 1975, Nuclear Scattering Radiography was introduced as a new method giving three-dimensional information on the matter distribution inside extended bodies. The first results[1] obtained on phantoms and on a chicken egg permitted a resolution of 10 mm^3 with reasonable hope of some sensitivity to the relative concentration of different elements like hydrogen, carbon, or oxygen.

Further work[2] at CERN with carbon, paraffin and water phantoms permitted a volume resolution of 2 mm^3 to be reached. The separation of hydrogen from heavier elements was shown to be almost perfect. Some preliminary measurements on animals were performed, with a volume resolution of 43 mm^3 only limited by the statistics permitted by the data acquisition system. First experiments with human tissues were undertaken at Saclay with high-accuracy drift chambers for particle localization. The results showed the capability of the method to clearly separate the scattering from the marrow and the bones in a spinal cord and gave a correct display of the structure of a sphenoid bone[3].

In the work presented here, a further step towards the exploitation of the method for the study of the human tissues has been made. A human head, preserved in a Formalin solution, has been investigated. Although the experimental conditions permitted the collection of data corresponding to an irradiation of only 0.3 rad, fruitful comparison could be made with the data from conventional X-ray computer-assisted tomography scans on the same material, with a more realistic evaluation of the intrinsic qualities of the method in the perspective of its clinical use.

PRINCIPLE OF THE METHOD

Various ways of using high-energy proton beams for radiography have been considered and tried in the last decade. They relied mostly on the following mechanisms: absorption by nuclear interactions, giving a shaded radiograph similar to the one obtained with X-rays[4]; the rapid change of energy loss near the end of the range[4]; and Coulomb scattering[5]. Various studies with human tissues have been performed with the second method, which is the most sensitive[6].

The first method has been considered for a system of computer-assisted tomography (CT), with the X-rays replaced by proton beams, and was the object of several feasibility studies -- the latest at Los Alamos[7] arriving at the conclusion of a definite dose advantage for the proton absorption method as compared with X-rays, by a factor close to 4 for a 20 cm thick object. In this approach, proton scans are treated like X-ray beams and measurements under a considerable number of angles are necessary to obtain tomographic information. The method presented here relies also on nuclear interaction, but one of its attractive features is to yield a three-dimensional view of the density distribution without any relative rotation or displacement of the beam and the object.

When protons in the 1 GeV energy range are scattered by matter the large-angle deflections are produced mainly by the nuclear collisions of the proton on the protons or neutrons bound in the nuclei contained in the molecules of the object. The binding energies of these nucleons, of the order of a few MeV, are relatively small with respect to the energy of impinging protons and the collision, called quasi-elastic, has nearly the character of an elastic encounter between particles of the same mass. By measuring the trajectories of the incoming and outgoing charged particles, one obtains the space coordinates of the interaction vertices whose density distribution reflects the matter distribution in the bombarded body (Fig. 1).

The trajectories are obtained from routine techniques in high-energy physics, i.e. proportional chambers, or drift chambers, permitting an accuracy of better than 1 mm in the coordinate measurement. More specific characteristics of the nuclear scattering interaction are given in the next section.

QUASI-ELASTIC PROTON SCATTERING

When protons of 1 GeV are scattered by nuclei the spectral distribution of the scattering protons is characterized by a small contribution of coherent elastic scattering by the whole nucleus and a broad peak from the quasi-elastic scattering on bound nucleons. Figure 2 shows some characteristic distributions at various angles for 1 GeV protons scattering on carbon[8].

The missing energy is transferred to the recoiling nucleon. For energy transfers larger than 150 MeV a knocked-out proton has enough energy to exit from a 20 cm thick tissue. This is the case for more than 50% of the recoil protons for a scattering angle larger than 16° experienced by a 1 GeV proton.

For an incident flux of N protons per unit area the number N_S of scattered protons by volume element V is given by:

$$N_S = 0.6\ NV\rho\sigma A\ ,$$

where ρ is the density of the target of atomic mass A and σ the nuclear scattering cross-section corresponding to A.

The cross-sections relevant to the process are:

$\sigma_{el}(H)$: elastic proton scattering from hydrogen (A = 1)

$\sigma_q(A_i)$: quasi-elastic scattering of protons from element A_i.

Thus for a molecule of type $(A_i)_{a_i}H_b$, of molecular mass M, the number of scattered protons becomes

$$N_S = 0.6\ NV\rho\ \frac{\sum a_i\sigma_q(A_i)}{M}$$

The motion of the nucleons bound in the nuclei results in a random momentum distribution, permitting a sharp distinction between the quasi-elastic scattering of protons on bound protons and on free hydrogen. In the last case momentum-conservation laws lead to two constraints:

- the scattered and recoil protons are coplanar with the incident proton;
- the angles θ_1 and θ_2, of the momenta of the two outgoing protons with respect to the direction of the incoming proton, obey the relation

$$\text{tg}\ \theta_1\ \text{tg}\ \theta_2 = k\ .$$

Figures 3a and b, obtained from scattering data of protons on a water phantom of 1 ℓ, illustrate the sharp difference between scattering on oxygen and hydrogen.

In the experimental conditions of Fig. 3 the hydrogen events would be separated with a residual contamination of only 5% from quasi-elastic scattering events on the protons bound in oxygen. The number of hydrogen events is

$$N_S(H) = 0.6\ NV\rho\ \frac{b\sigma_{el}(H)}{M}\ .$$

The quantities N_S and $N_S(H)$ are all proportional to the density of the target and can be used to sample the density distribution. The ratio $N_S(H)/N_S$ is independent of density and depends on the relative concentrations of hydrogen and heavier elements.

SPATIAL RESOLUTION AND DOSE LIMITATIONS

The volume resolution is limited by several factors: the accuracy in the determination of the particle trajectories, the multiple Coulomb scattering, and the minimum deflection angle accepted for the scattered particle. The errors in the plane orthogonal to the beam direction are amplified by a factor $1/\sin\theta_1$ in the z direction. For this reason scattering angles below 15° were excluded.

While drift chambers could permit a localization accuracy of about 0.1 mm, we have chosen for reasons of speed to use a multiwire chamber with a wire spacing of 1.27 mm for the incoming beam and 2 mm for the outgoing particles. This limits the accuracy (FWHM) to about 1 mm in the (X,Y) plane and 4 mm in the Z plane. The instrumentation then permits a volume resolution of 4 mm^3.

The incoming and outgoing protons are deflected by the electric field of the target nuclei. This phenomenon, called multiple Coulomb scattering, has been extensively studied. The distribution of the projected angles of deflection, after passing a thickness of tissue of 10 cm, for a 1 GeV proton is about 0.5°. For a proton scattered at an angle of 20° in the middle of a 20 cm spherical body this would bring in a volume error of 3 mm^3. We thus see that the accuracy of our present instrument closely matches the uncertainty from Coulomb scattering. It is clear that to exploit this accuracy it is necessary also to have an adequate statistical accuracy, i.e. enough events in each volume element, and this is where the dose limitation enters as a limiting factor to accuracy.

Our first analysis[1)] gave a table of the correlation between the precision of the elementary volume and the doses. It was based purely on the statistical accuracy

inside every volume bin without taking into account the correlation between adjacent bins and the techniques of deconvolution common in image processing. It also did not take into account the particles lost by absorption.

In view of our present experience this evaluation has to be corrected, as will be shown in the discussion of our results, and Table 1 gives our present evaluation of the doses for different choices of precision for 1 GeV protons, for a quasi-perfect system.

EXPERIMENTAL SET-UP

The human head, conserved in a Formalin solution, was placed in a low-density styrofoam cradle of density 0.03 g/cm^3, inside a lucite box. The matter outside the target is thus kept to a minimum, simulating as closely as possible the conditions of an *in vivo* radiography. Figure 1 shows the experimental set-up. Auxiliary scintillation counters are used to preselect grossly the events of interest. The coincidence between SC_1 and SC_2 in the incident proton beam determines the useful part of the target. SC_3 determines the maximum acceptance of the scattered particles, while SC_4 and SC_5 in anticoincidence reject those particles which have not been scattered or have been deflected by too small an angle. The proportional chamber CH_4 was set at 65 cm from the centre of the target, thus permitting the measurement of particles deflected up to 40°, which corresponds to an acceptance angle of 1.1 sr, taking into account the small deflection angle rejection. The corners of CH_4 were inefficient in order to have the maximal angle roughly independent of the azimuth. In the case of a deflection in hydrogen, CH_4 detects only one of the two recoiling protons. This simplifies the data treatment without any loss in accuracy in the absence of a strong background.

The time resolution of the preselection scintillation telescope was 10 ns, while the resolution of the chamber was 100 ns. With the beam intensities handled in this experiment, 10^5/s maximum, these resolutions kept the accidentals at a negligible level.

ON-LINE DATA TREATMENT

The information from the chambers is stored in the buffer of the computer HP 21 MXE, fitted with a 16-bit 32-kiloword memory, with micro-instructions increasing the treatment speed. The treatment starting after the end of the storage process consisted in a selection of the good events and the determination, for those only, of the coordinates of the intersection points of the trajectories. When two particles are detected in CH_3, with angles θ_1 and θ_2, a coplanarity test is made and the quantity tg θ_1 tg θ_2 computed. This information (X, Y, Z and occasionally tg θ_1 tg θ_2) is stored on tape. The treatment time for a single event was 260 μs. The maximum acquisition rate was 2500 events per cycle, out of which 1500 good events could be extracted. Among the selection criteria was the requirement for the scattering angle to be greater than 16°.

RAW DATA TREATMENT

The events written on tape are stored in a matrix of 96 slices of 124 × 124 cells of 1.4 mm in X and Y, and 2.8 mm in Z, i.e. all together 1.5×10^6 cells of an elementary volume of 5.5 mm^3.

As a first step, we corrected this matrix for the intensity distortions introduced by the beam non-uniformity, and the attenuation in the target of the incident and emerging protons. This correction was obtained by regrouping the events into grosser cells, namely cubes of 8.4 mm side, selecting only cells having no bones and fitting their distribution by a quadratic function:

$$F(X,Y,Z) = \sum_{i=0}^{i=2} \sum_{j=0}^{2} \sum_{k=0}^{2} C_{ijk} Z^k Y^i X^i \ ,$$

reproducing the slow variations in the target. The maximum correction was about 20%; the r.m.s. deviation between this function and the real intensity was 4%. The result of this correction appears clearly in Fig. 4, where we plot the density spectra of the cells inside a 11.2 mm thick slice corresponding to a summation over 4 elementary slices in the matrix. Figure 4a corresponds to the non-corrected matrix for which the vertex densities in soft tissues are distributed in a peak

of 30% FWHM, while the bones appear as a tail in the high density side. Figure 4b shows the same spectrum with the corrected matrix. The soft tissue spread has been reduced to 13%, while the purely statistical spread per cell is 11%. The bones now appear as a distinct peak.

The next step in the data handling consists of a two-dimensional smoothing in the XY slices which brings down the statistical effect to 2.5% at the cost of loss in spatial resolution. The effect on the data is visible in Fig. 4c; the soft tissue spread is now only 5.5%, well above the statistical spread.

The results which we present correspond to this level of treatment. They show the main characteristics of the method prior to any image treatment, which should also be capable of improving the image quality.

EXPERIMENTAL RESULTS

The irradiation lasted four days and the dose was about 0.3 rad. One hundred and thirty million simple events N_S were stored in a three-dimensional matrix M(X,Y,Z). In our case, horizontal, frontal, and sagittal slices of the head correspond, respectively, to the XY, ZX, and ZY planes (see Fig. 1). About 100 scattered events are stored per volume element (vel) for soft tissues. Elementary planes may be summed in order to increase this number and improve the sensitivity. For hydrogen radiographs about seven million events are obtained. To visualize the slices we use linear convention: pixels on the image have grey tones going from black to white when N_S or $N_S(H)$ increases.

For this study a head preserved in Formalin was examined by proton tomography and an X-ray scanner. Horizontal sections of the specimen were radiographed and photographed.

Proton tomography yields 11.2 mm thick sections in the horizontal plane (XY) and the X-ray scanner (EMI 10/10) 10 mm thick sections. The thickness of the anatomical slices was also 10 mm.

Coronal sections and sagittal sections were both 5.6 mm thick with proton CT. A Formalin-preserved specimen presents the worst conditions of examination on

account of tissue modifications during the fixation process. However it was the only method to compare successive CT scans and anatomical sections of the same specimen.

Artifacts due to the fixation of tissues appear on the images of proton CT and X-ray CT scans. For the horizontal sections, the comparison of the two methods emphasizes the results showing the differentiation between simple and hydrogen structures.

PROTON TOMOGRAPHY OF HORIZONTAL SECTIONS (Fig. 5)

We obtained 18 sections from the base to the vertex. Compared with other conventional techniques, bone structures present a less dense barrier.

The inferior sections 13-16, 17-20, 21-24 correspond to the lower area and the roof of the mouth.

The sections 25-28, 29-33, 33-36, 37-40 correspond to the maxillary sinus and the upper cervical area.

Sections 45-48, 45-52 show the base of the orbit cavities.

The superior sections pass through the white matter of the hemispheres, the basal ganglia, and the cerebral cortex.

Fixation artifacts at the level of the frontal lobe are due to a cerebral detachment.

CORONAL SECTIONS (Figs. 6, 7)

There are 30 sections in the ZY plane, corresponding frontwards to the frontal area, the nasal cavity, the ethmoid and the orbit area, backwards on sections 33-36, 37-40 to the sella and the temporal fossa. Sections 65-68, 109-112 analyse the petrous bone, the occipital fossa and the cervico-occipital area. The images of the cerebral structures are not very clear because of fixation artifacts and lack of smoothing.

SAGITTAL SECTIONS (Figs. 8, 9)

The same difficulties occur with the sagittal sections. The midline section 61-64 analyses the sella turcica.

COMPARISON OF THE METHODS

Proton CT images have been compared with X-ray scanner images. The bone structures are more clearly analysed by X-ray because of a higher absorption coefficient. The analysis of horizontal sections gives interesting results on the scattering of hydrogen elements, and their differentiation. The bone which contains less hydrogen disappears and we can obtain real CT subtractions at the level of the skull base showing only the cerebellum and the temporal lobes (hydrogen images 45-48, 49-52).

At the level of the foramen magnum, the subarachnoid spaces and the cervical cord are well visualized, while the bone structures of the foramen and the odontoid process are erased (section 41-44).

Around the brain, the image corresponds to the ambient milieu of Formalin and cotton wool.

ANATOMICAL CONFRONTATIONS

A series of 12 horizontal sections near the orbito-meatal plane, was made in the cranial specimen. The sections were photographed and radiographed on metallographic films. The comparison of the reconstructed images is only possible for horizontal sections.

As regards the figures, the sections chosen are representative of a given area.

The 1st section (Fig. 10) shows the level of the sub-occipital junction and gives a good definition of the cervical cord in the bone canal surrounded by the subarachnoid spaces filled with CSF. The 2nd section (Fig. 11) passes through the posterior fossa and frontwards through the orbits. It shows the cerebellar hemispheres, the fourth ventricle, and the brainstem.

The 3rd section (Fig. 12) is made through the hemispheres at the level of the basal ganglia (thalamus, lenticula, caudate nucleus), the wide pathways of the white matter in the internal capsule, and the centrum ovale.

The 4th and last section (Fig. 13) near the vertex determines the sulci and convolutions on the convexity of the brain and passes through the falx-cerebri.

By comparison it is also possible to determine the absorption coefficient and to show the richest structures in hydrogen at the level of a section. At the level of the bone, the diagrams are similar and hydrogen shows hypodensity. With an arbitrary 3% variation unit the value and the variations of hydrogen structures are 3 or 4 times higher than with the proton method. Therefore the variations which do not appear on CT scans, with the simple proton examination, may be shown by the hydrogen.

Figure 14 shows a comparison of simple and hydrogen radiographs for eight horizontal slices. We combine these two types of radiographs in Fig. 15, where we show simple (N_S) and hydrogen $N_S(H)$ radiographs and their combination $N_S(H)/N_S$, $N_S/N_S(H)$ and $N_S \times N_S(H)$ for one horizontal slice. To be more quantitative we give the histograms of the counting rate as a function of the position along the horizontal lines. On S and H radiographs bone appears, respectively, in white and black. This is explained by the low percentage[4] in weight of hydrogen in bone ($\sim$ 6%) compared with soft tissue (11%). Taking in a crude approximation the atomic compositions[4], the densities, and the nuclear cross-sections involved, one may compute a contrast of about +30% between bone and smooth tissue for simple radiographs, and -13% for hydrogen radiographs. The measured values shown on the histograms are +25% and -15%. More interesting is the fact that in soft tissues, the contrast in the brain hypodensity varies from 6% to 15% for single and hydrogen radiographs, respectively. The difference of sensitivity of these two types of radiographs is promising. Figure 4 also shows an H/S radiograph which is density-independent. There, the bone appears with high contrast (about 35%), but the hypodensity contrast is well reduced. On the S × H radiograph, which is dependent on the square of the density, the bone contrast is reduced to about 10%, but the hypodensities appear very well (20% effect).

To give the sensitivity of the nuclear scattering radiography, we show in Fig. 16 some horizontal slices with a width of only 2.8 mm (the vel is then 5.5 mm^3). To decrease the statistical noise, we smooth each slice three times. The loss in spatial resolution is clearly visible on the bone which has a larger spread than in Fig. 5. Figure 17 shows a comparison of horizontal slices obtained by proton radiography and the X-ray CT scanner. The two hypodensities detected by the X-ray scanner in the two brain hemispheres are also visualized by protons despite a dose delivery five times lower.

PROSPECTS OF EXPERIMENTATION WITH LIVING HUMANS

These results have been obtained with a low irradiation of 0.3 rad under experimental conditions where the total time for the data acquisition was 4 days. It is desirable to be able to reach a limiting tolerable dose of 2 rad, obtained in a time of the order of a few minutes. There is nothing in the present stage of technology which seems to prevent us from reaching these goals.

We have built a new data acquisition system, exploiting a beam of the improved version of the Saclay synchrotron accelerator, SATURNE. Among the factors that will allow us a large gain in acquisition spread as compared with our preceding experiment, we have:

- a gain of 3 in duty cycle as compared with the CERN accelerator;
- a gain in the resolution-time and dead-time of the circuits equipping the chamber: MOS circuits replaced by specially integrated ECL circuits;
- a gain in the speed and storage capacity of the memory;
- the implementation of a fast data acquisition system, using microprocessors and permitting the full treatment of an event in 10 μs as compared with the preceding 260 μs [9]. We expect to reach 10^8 events in less than 40 min. Further steps in improving the speed of data acquisition will be undertaken if the results obtained with living tissues appear to be as encouraging as foreseen.

ACKNOWLEDGEMENT

This work was carried out with the aid of INSERM grant No. CRL 78.5.014.6.

REFERENCES

1. Saudinos J, Charpak G, Sauli F, Townsend D, Vinciarelli S, Phys. Med. Biol. 20:890-905, 1975.

2. Charpak G, Majewski S, Perrin Y, Saudinos J, Sauli F, Townsend D, Vinciarelli J, Phys. Med. Biol. 21:941-948, 1976.

3. Berger J, Duchazeaubeneix JC, Faibre JC, Garreta D, Legrand D, Rouger M, Saudinos J, Raybaud C, Salamon G., J. Computer Assisted Tomography, October 1978.

4. Koehler AM, Science 160:303-305, 1968.

5. West D, Sherwood AC, Nature 239:157-159, 1972.

6. Steward VW, Koehler AM, Radiology 110:217, 1975.

7. Hanson KM, Development of a proton radiographic system for diagnosis and localization of soft-tissue abnormalities, Los Alamos final report LA-7107-MS, February 1978.

9. Bricaud B, Faivre JC, Pain J, SAR: a fast computer for CAMAC data acquisition, IEEE Trans. Nucl. Sci. NS-26:4641-4644, 1979.

Table 1

Approximate doses in rad

Elementary volume (mm^3)	Precision		
	0.5%	1%	5%
5	10	2.5	0.1
10	5	1.25	0.05

Figure captions

Fig. 1 : Nuclear scattering radiography. A proton of about 1 GeV, travelling along the Z axis is scattered by the nucleus of a target. It is deflected by an angle θ_1 with respect to Z. The recoiling nuclear neutron or proton is emitted at an angle θ_2 with respect to Z. The multiwire proportional chambers, CH_1, CH_2, CH_3, CH_4, two in front of and two after the target, determine the trajectories of all the charged particles and permit the calculation of the interaction vertex coordinates. The scintillation counters SC_1, SC_2, SC_3, SC_4, SC_5 select grossly the large-angle scattering events.

Fig. 2 : Energy distribution of 1 GeV protons scattered by a carbon target at various angles.

Fig. 3 : Separation between scattering on free and bound hydrogen.

Fig. 4 : Corrections to the vertex distribution density.

a) Raw density distribution without correction.

b) Density distribution after correction for beam non-uniformity and particle absorption, using a quadratic correction function.

c) Density distribution after a smoothing consisting in averaging in two consecutive bins.

Fig. 5 : Horizontal slices. The width is 11.2 mm.

Figs. 6,7 : Frontal slices with a width of 5.6 mm.

Figs. 8,9 : Sagittal slices. The width is 5.6 mm.

Fig. 10 : Horizontal section of the skull: photograph (A) and radiograph (B). The plane of the section passes through the cervical cord (1), the medullary spinal spaces (2), and the second cervical vertebra (3). It shows the ascending parts of the inferior maxillary (4) and frontwards the inferior part of both maxillary sinuses.

Fig. 11 : Horizontal section (4 cm higher than Fig. 10): photograph (A) and radiograph (B). Backwards the section passes through the squamous part of the occipital bone (1), laterally through the petrous bones (2), and frontwards through the temporal fossa (3), the orbital cavities (4) and the nasal fossa (5). The most important cerebral structures are the brainstem (6), the fourth ventricle (7), the vermis (8), the cerebellar hemispheres (9), the globes of the eyes (10), and the optic nerves (11).

Fig. 12 : Horizontal section (3 cm higher than Fig. 11): photograph (A) and radiograph (B). The section through the cerebral hemispheres determines a great number of structures: Lateral ventricles (1), caudate nucleus (2), putamen (3), internal capsula (4), thalamus (5), corpus callosum (6), white matter (7), interhemispheric fissure (8), insula (9), cerebral cortex of the frontal lobe (10), cerebral cortex of the parietal lobe (11), cerebral cortex of the occipital lobe (12)

Fig. 13 : Horizontal section next to the vertex (4 cm above Fig. 12): photograph (A) and radiograph (B). The sulci on the convexity of the brain are clearly displayed (1) in relation to the cerebral cortex (2). The very thin falx cerebri separates both hemispheres (3). The bone shows an abnormal thickness because of its obliquity in relation to the section (4).

Fig. 14 : Comparison of simple and hydrogen radiographs for 8 horizontal slices.

Fig. 15 : Comparison of simple (S) and hydrogen (H) radiographs and their combinations in the case of a horizontal slice. Histograms give a qualitative evaluation of the different contrasts.

Fig. 16 : Horizontal slices with a width of 2.8 mm. Each slice is smoothed three times.

Fig. 17 : Comparison of almost identical slices obtained by proton radiography and X-ray CT scanner. In the proton radiography, the dose delivery is five times lower.

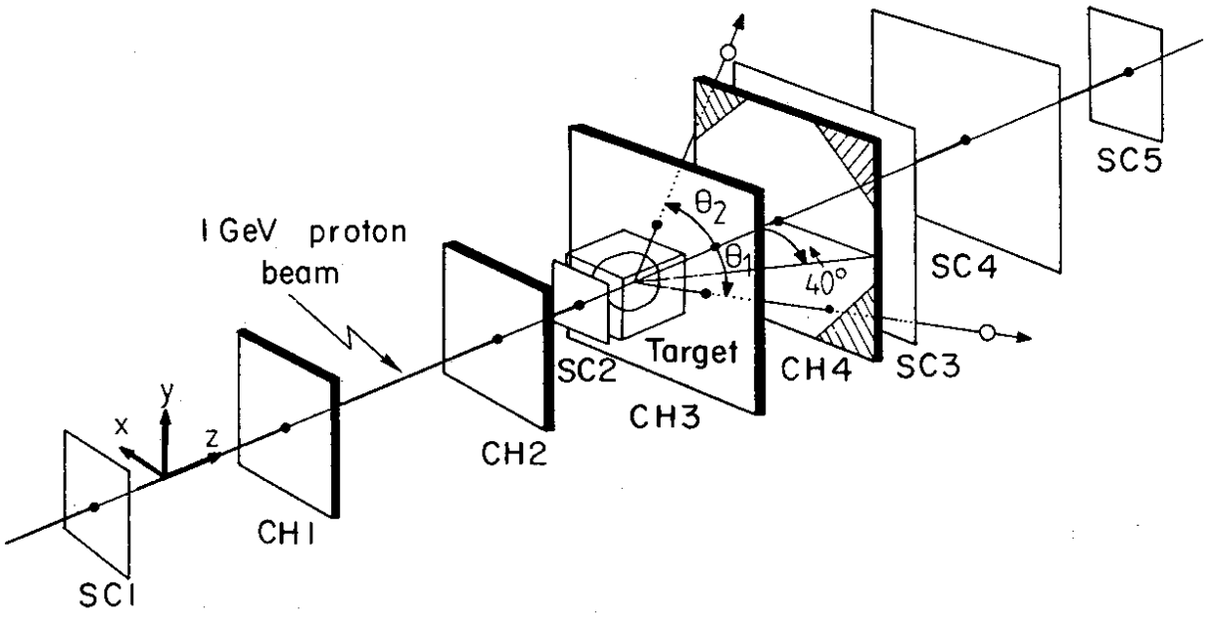
1 GeV proton
beam
SC1
CH1
CH2
SC2
Target
CH3
CH4
SC3
SC4
SC5
θ2
θ1
40°
x
y
z

Fig. 1

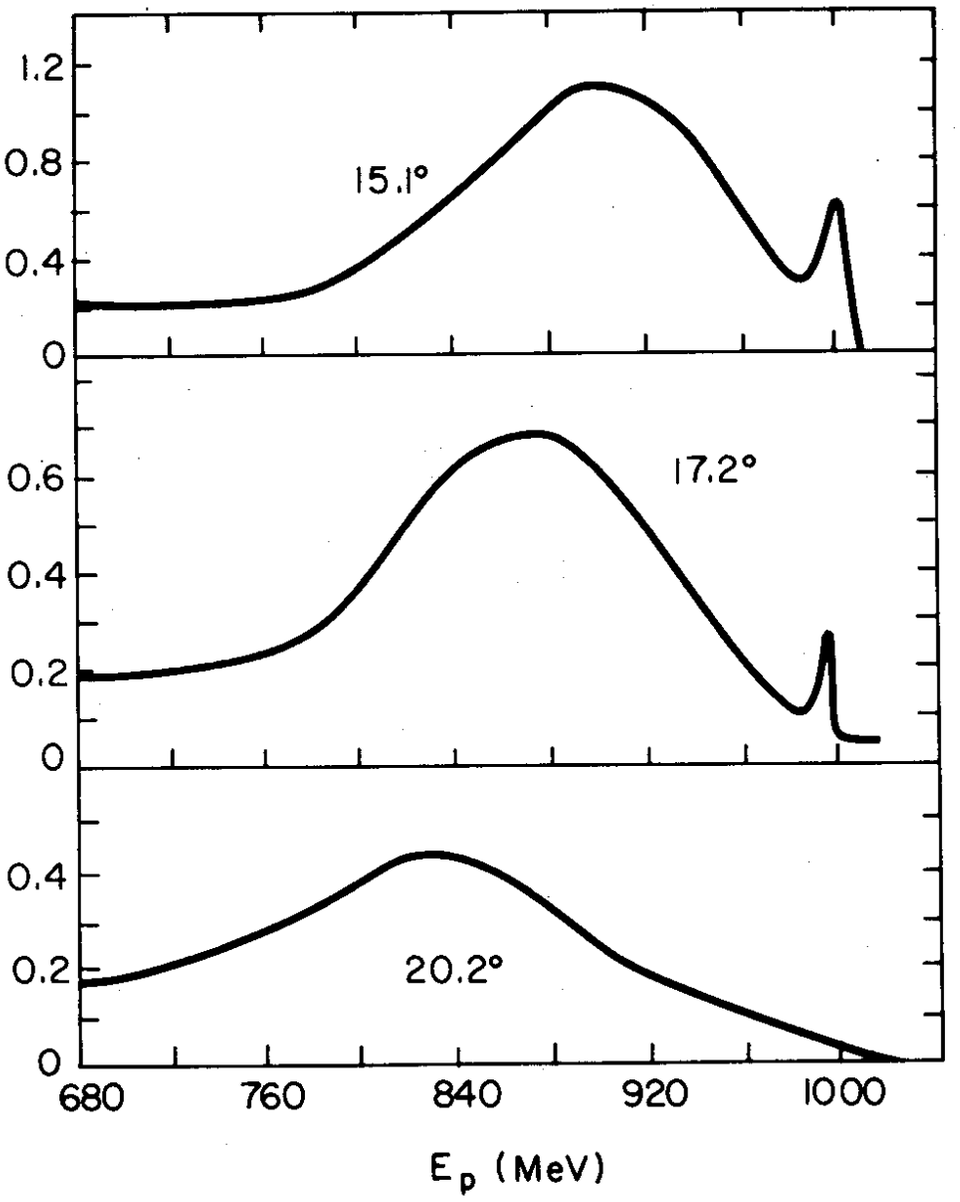

Fig. 2

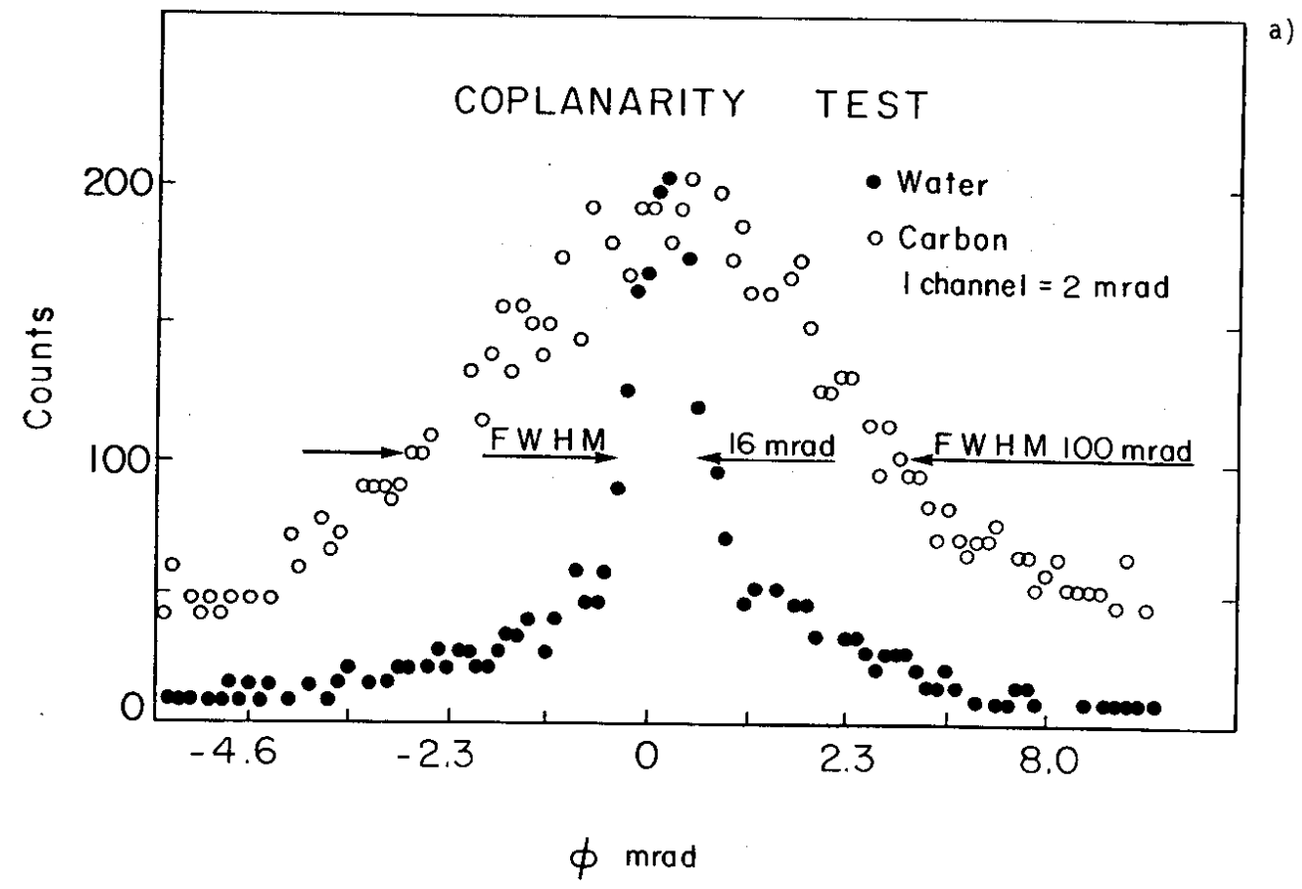
a)
COPLANARITY TEST
Water
Carbon
1 channel = 2 mrad
Counts
200
100
0
FWHM
16 mrad
FWHM 100 mrad
-4.6
-2.3
0
2.3
8.0
φ mrad

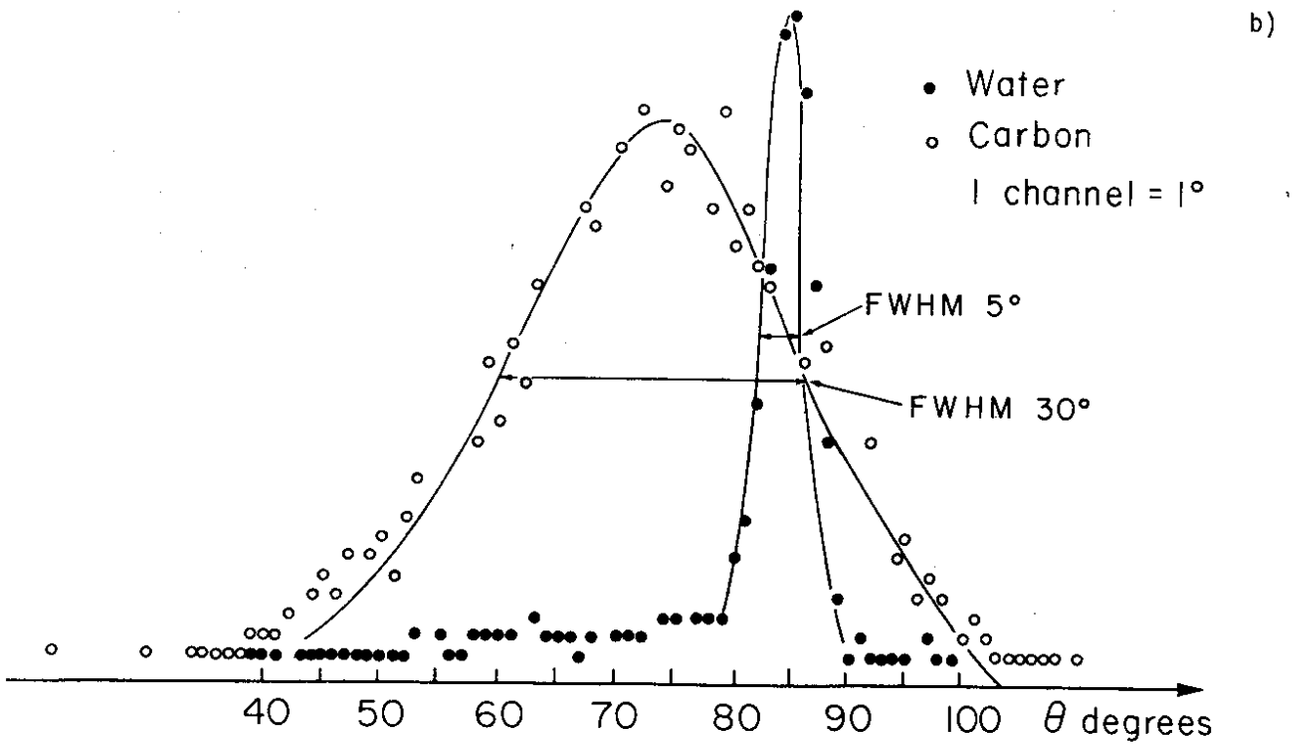
b)
Water
Carbon
1 channel = 1°
FWHM 5°
FWHM 30°
40
50
60
70
80
90
100
θ degrees

Fig. 3

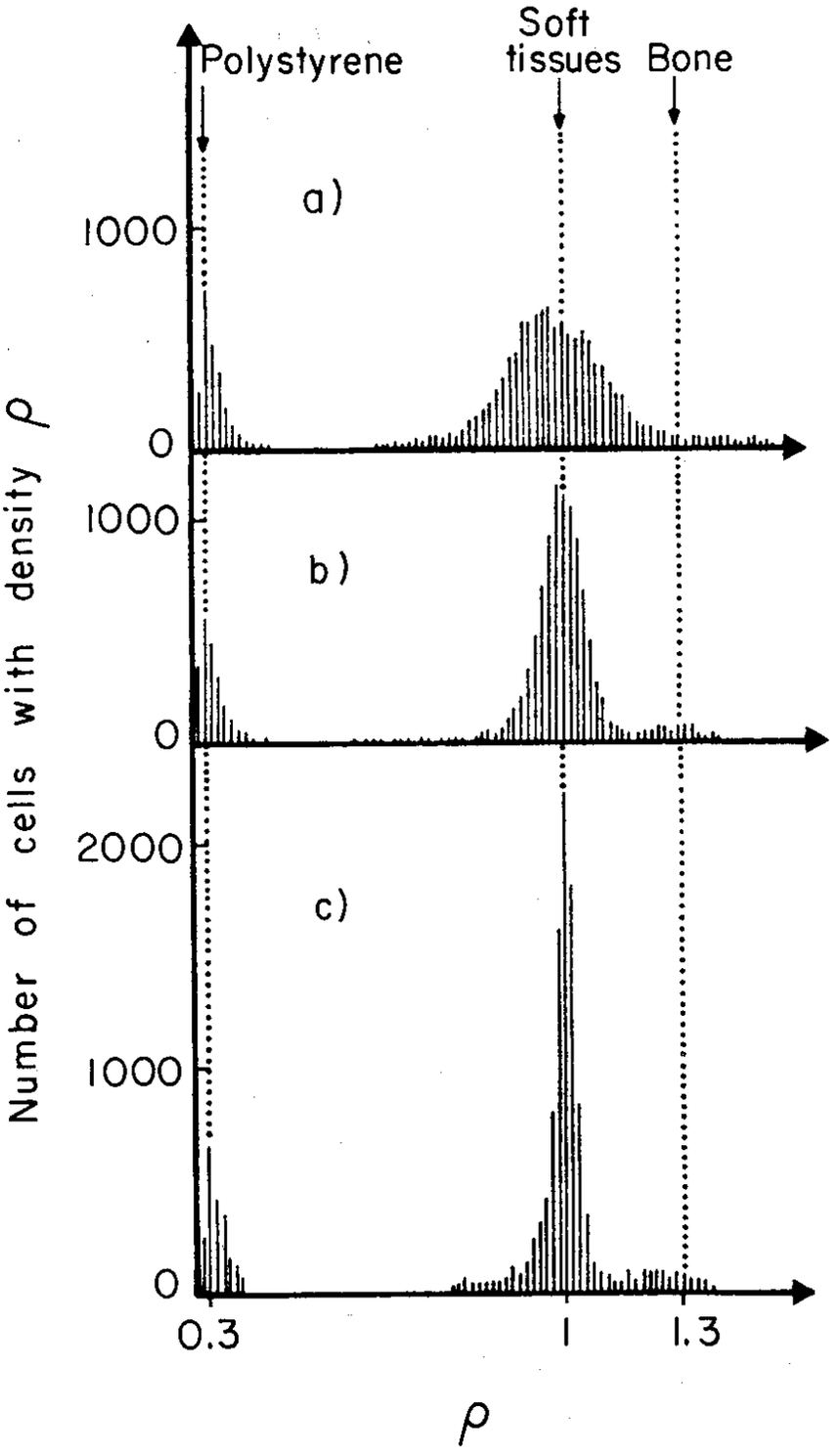
Polystyrene
Soft tissues
Bone
a)
b)
c)
1000
0
1000
0
2000
1000
0
0.3
1
1.3
ρ
Number of cells with density ρ

Fig. 4

XY - SIMPLE

PIXEL : 1.4 x 1.4 mm^2

VEL : 22 mm^3

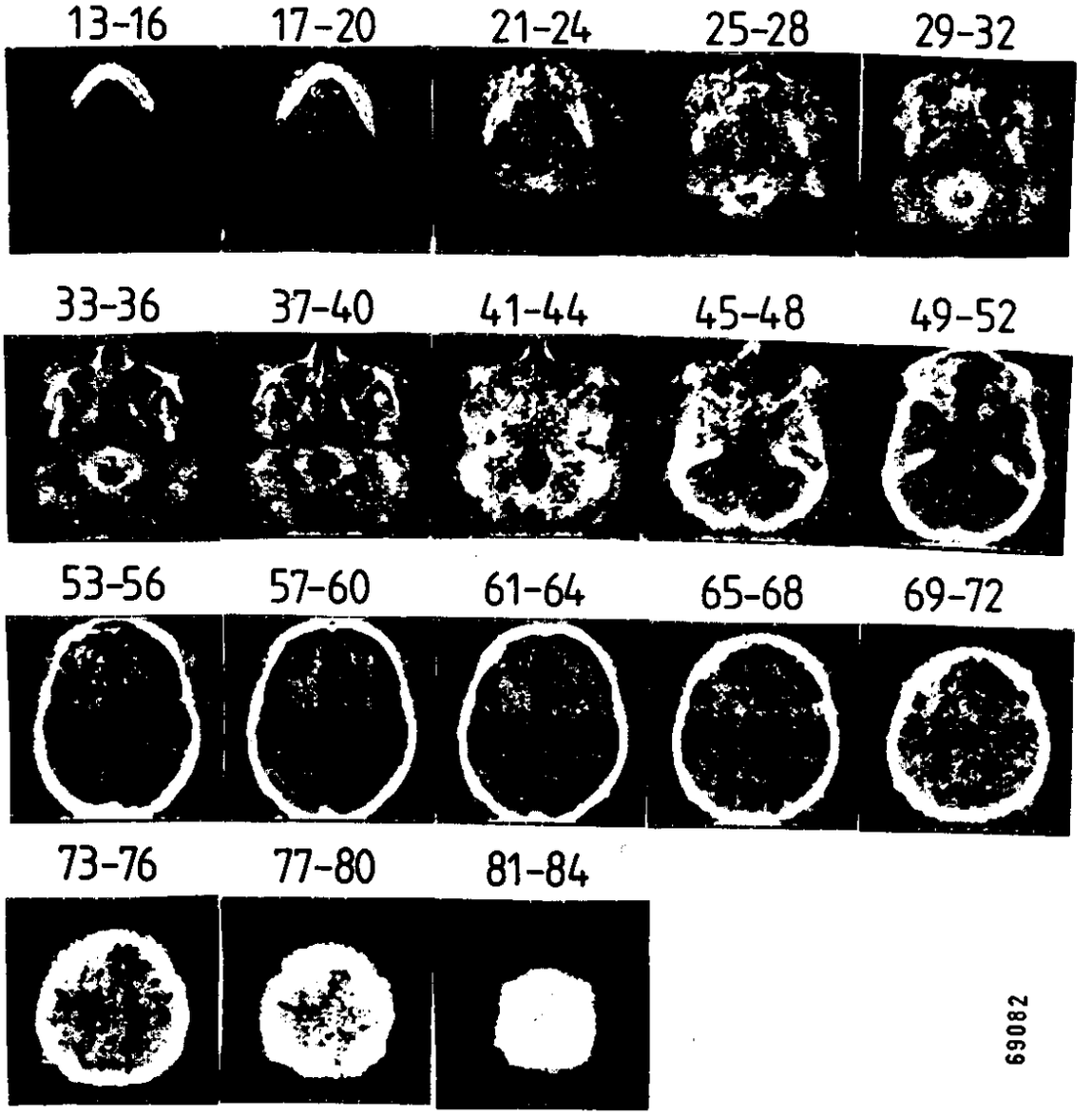

69082

Fig. 5

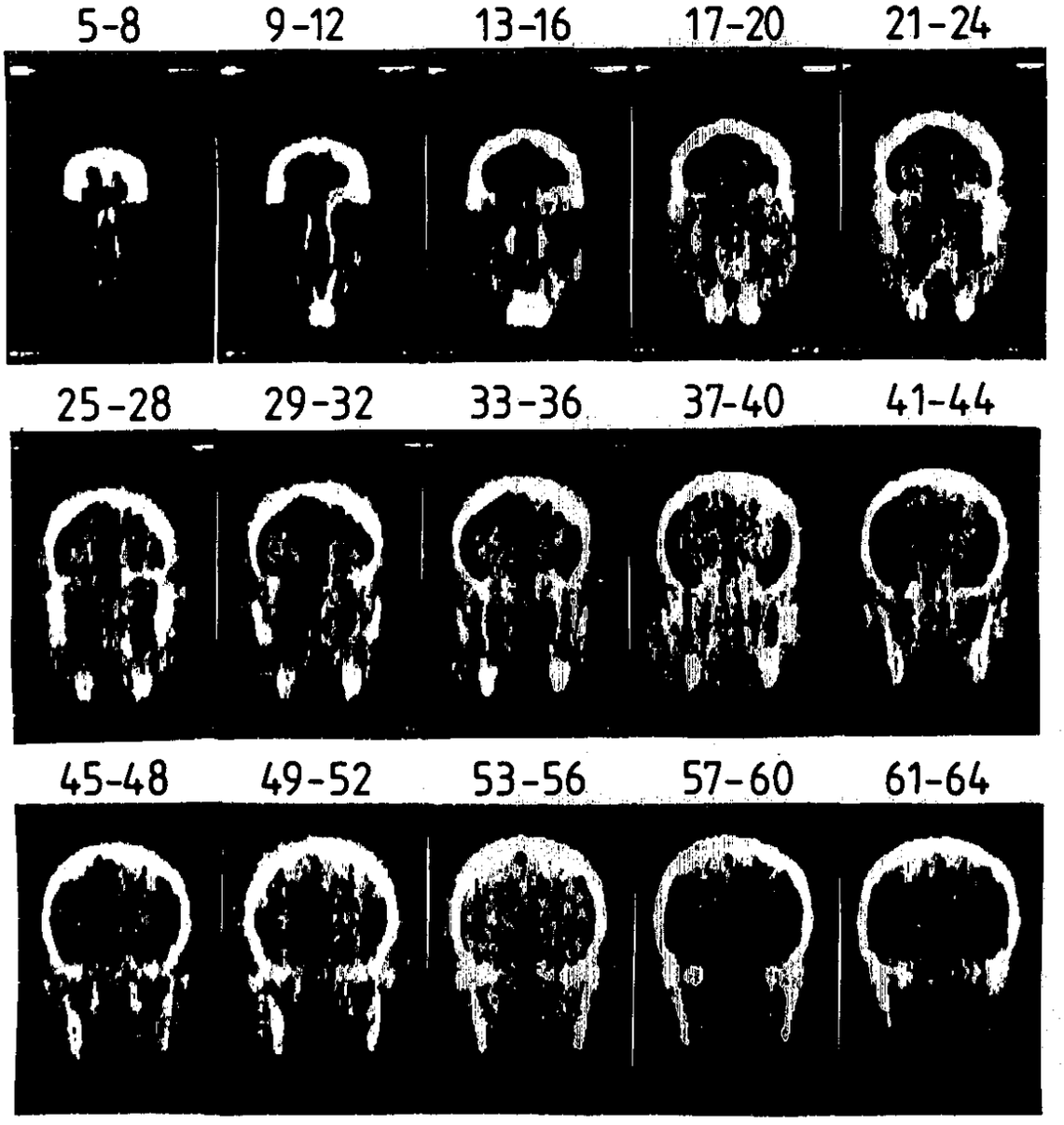
ZX - SIMPLE
PIXEL : 1.4 × 2.8 mm²
VEL : 22 mm³
5-8
9-12
13-16
17-20
21-24
25-28
29-32
33-36
37-40
41-44
45-48
49-52
53-56
57-60
61-64
69079

Fig. 6

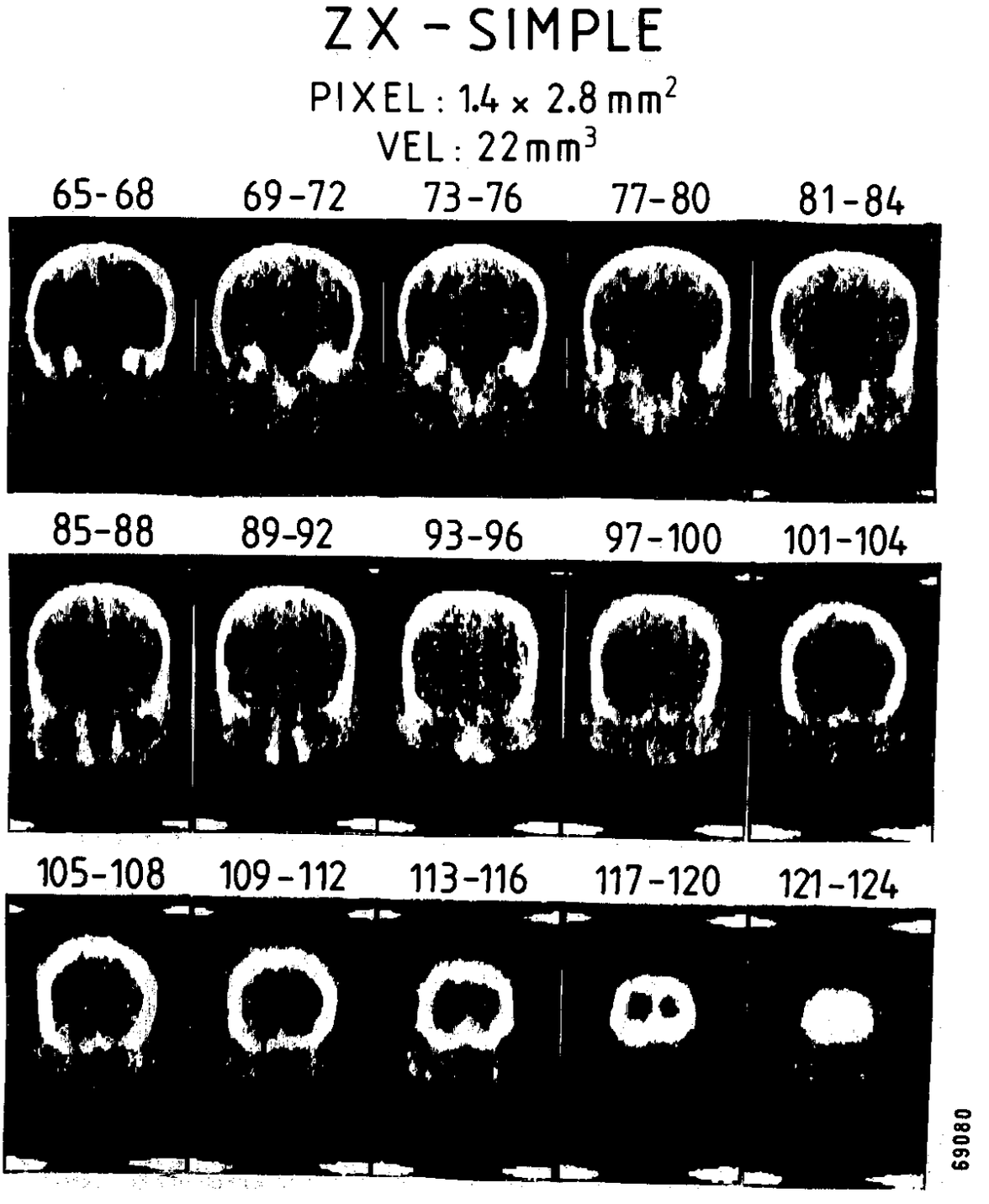
ZX - SIMPLE
PIXEL : 1.4 x 2.8 mm²
VEL : 22 mm³
65-68
69-72
73-76
77-80
81-84
85-88
89-92
93-96
97-100
101-104
105-108
109-112
113-116
117-120
121-124
69080

Fig. 7

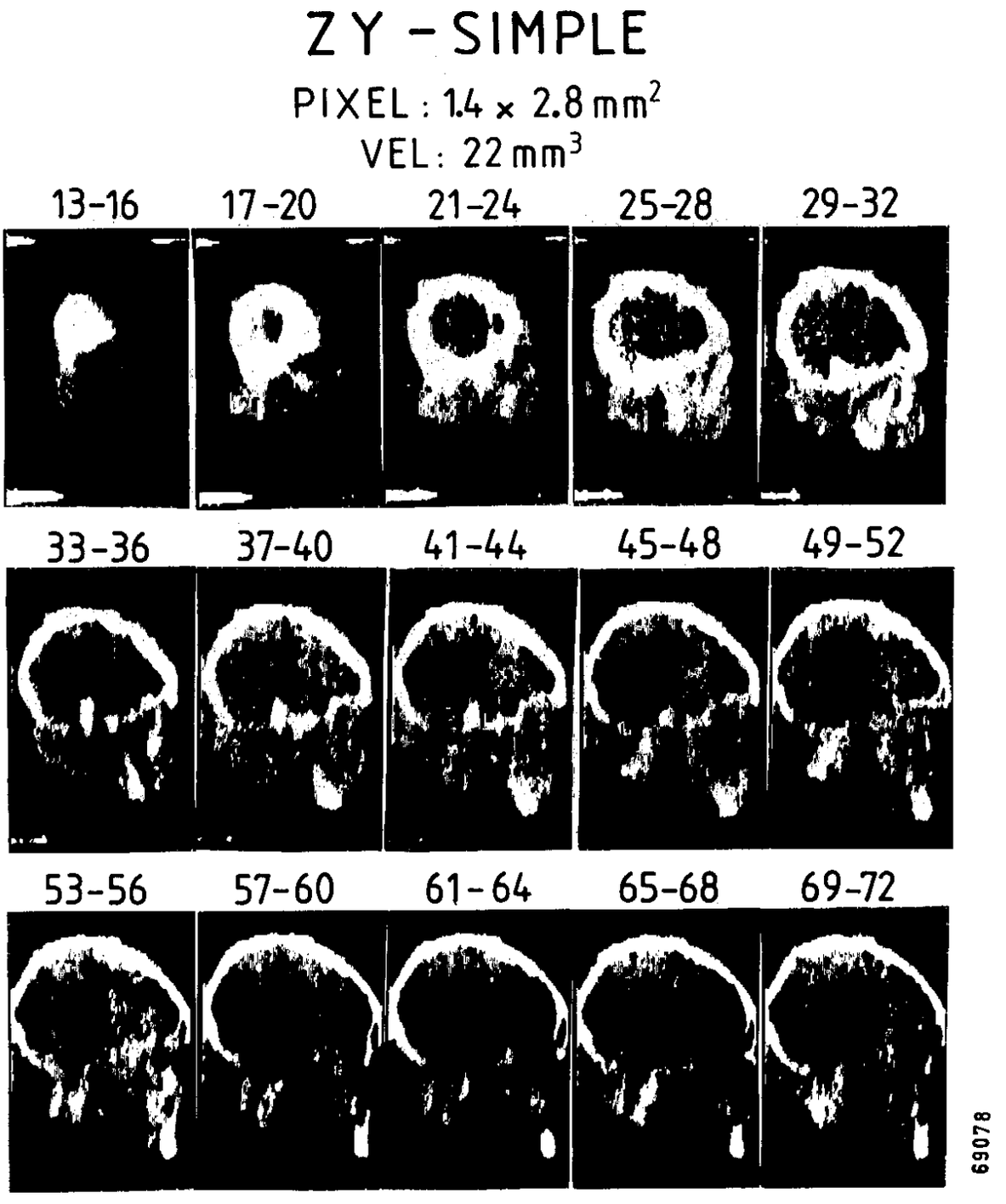
ZY - SIMPLE
PIXEL : 1.4 x 2.8 mm²
VEL : 22 mm³
13-16
17-20
21-24
25-28
29-32
33-36
37-40
41-44
45-48
49-52
53-56
57-60
61-64
65-68
69-72
69078

Fig. 8

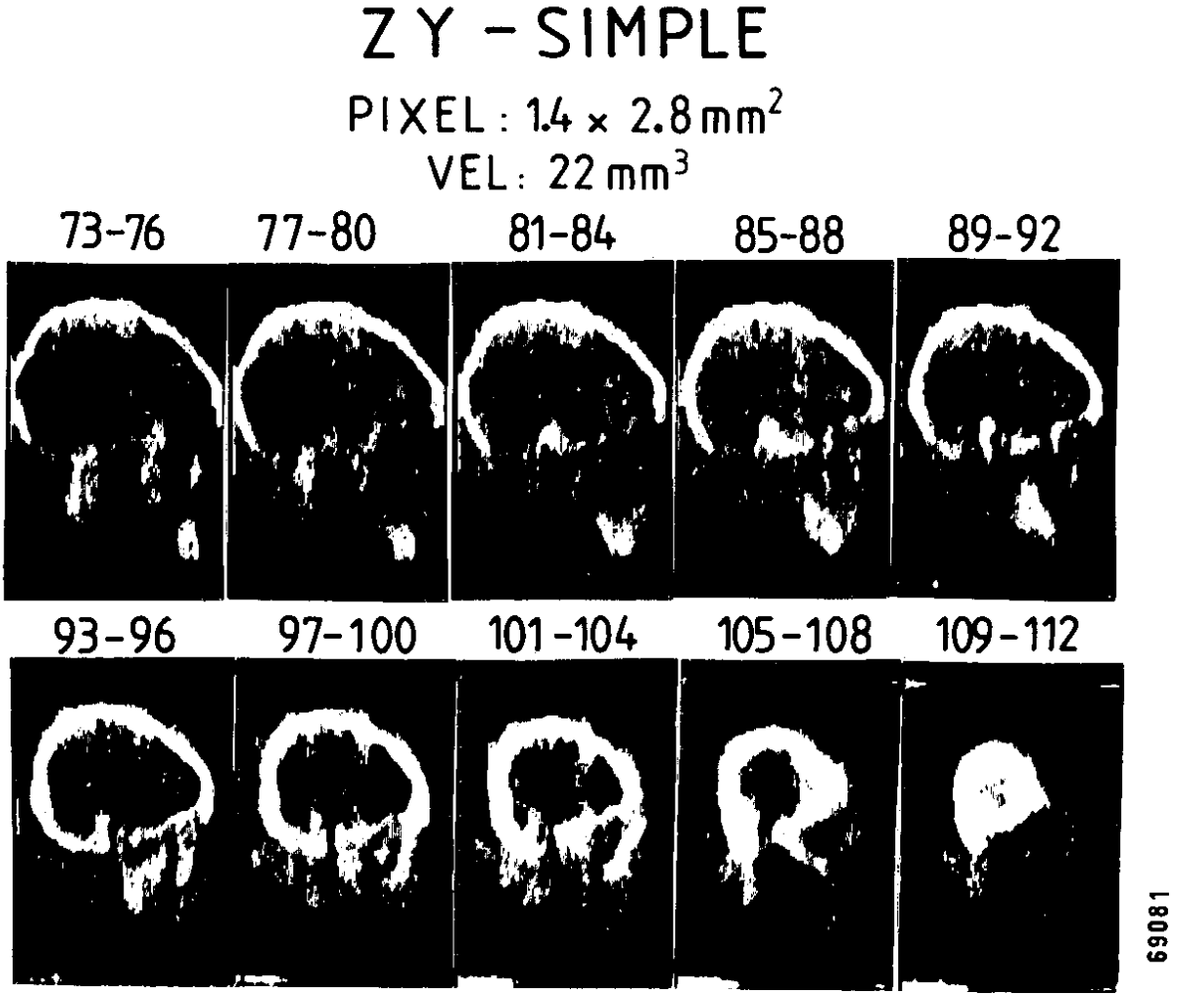
ZY - SIMPLE
PIXEL : 1.4 x 2.8 mm²
VEL : 22 mm³
73-76
77-80
81-84
85-88
89-92
93-96
97-100
101-104
105-108
109-112
69081

Fig. 9

Fig. 10

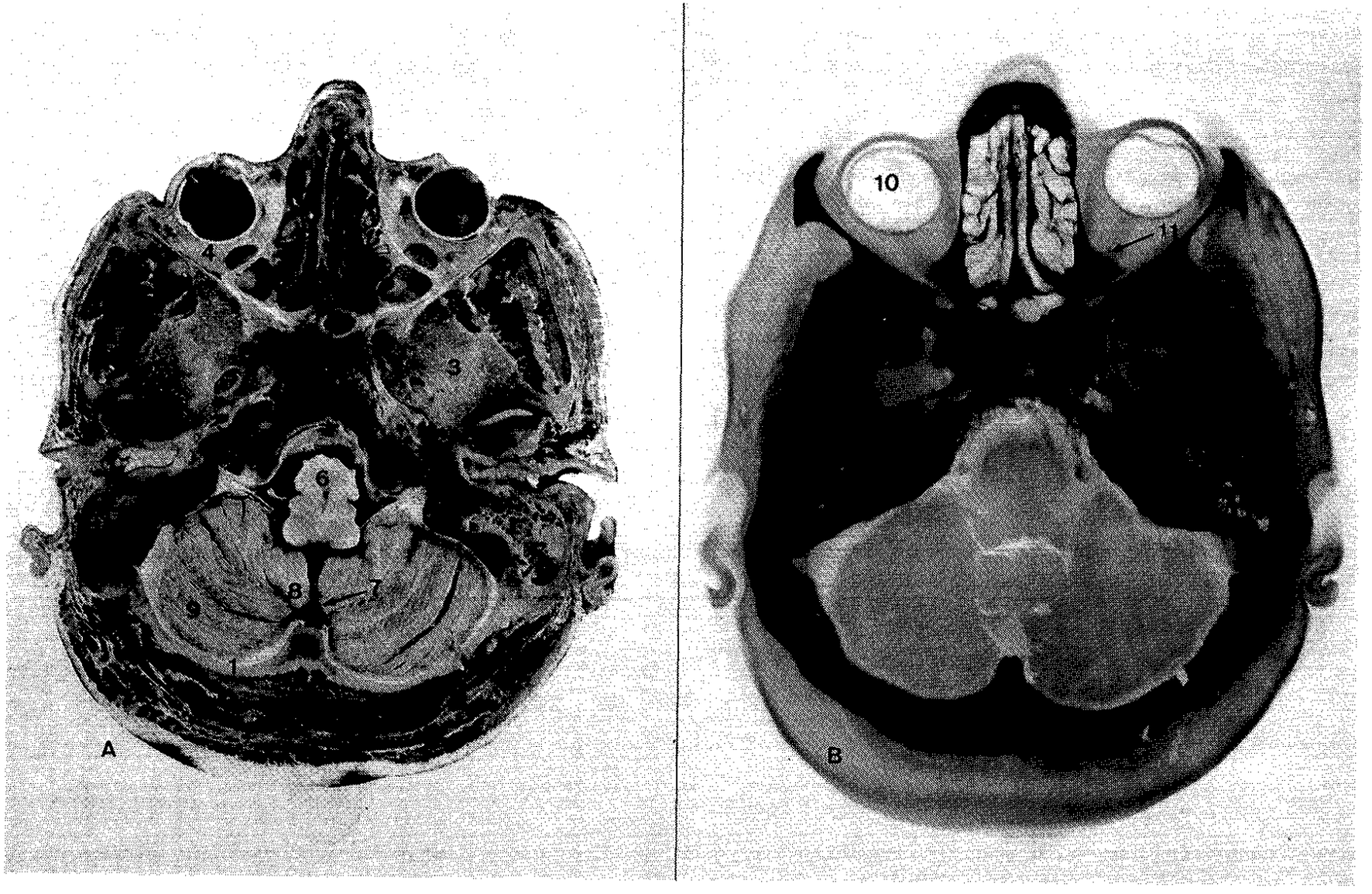

Fig. 11

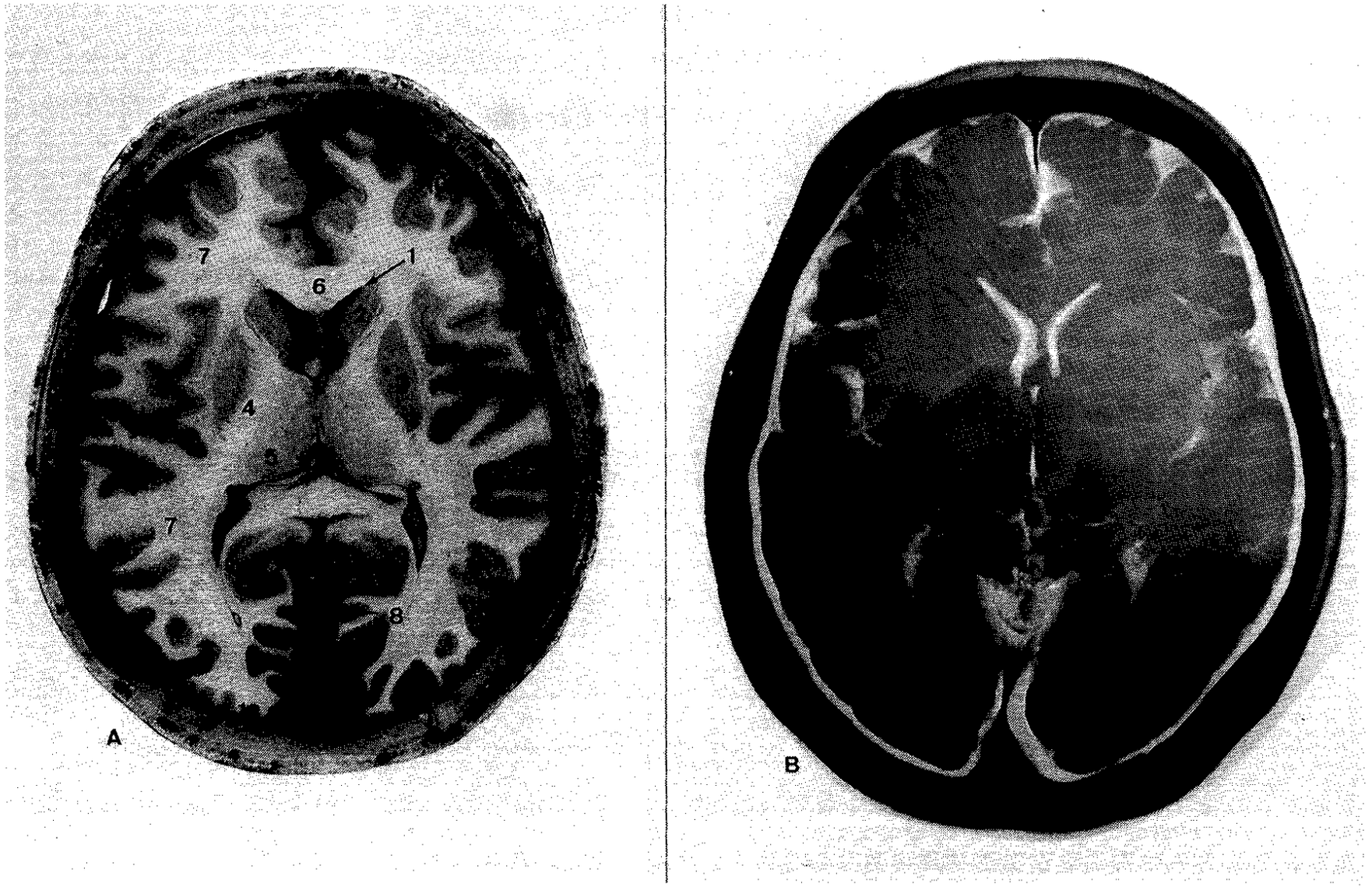

Fig. 12

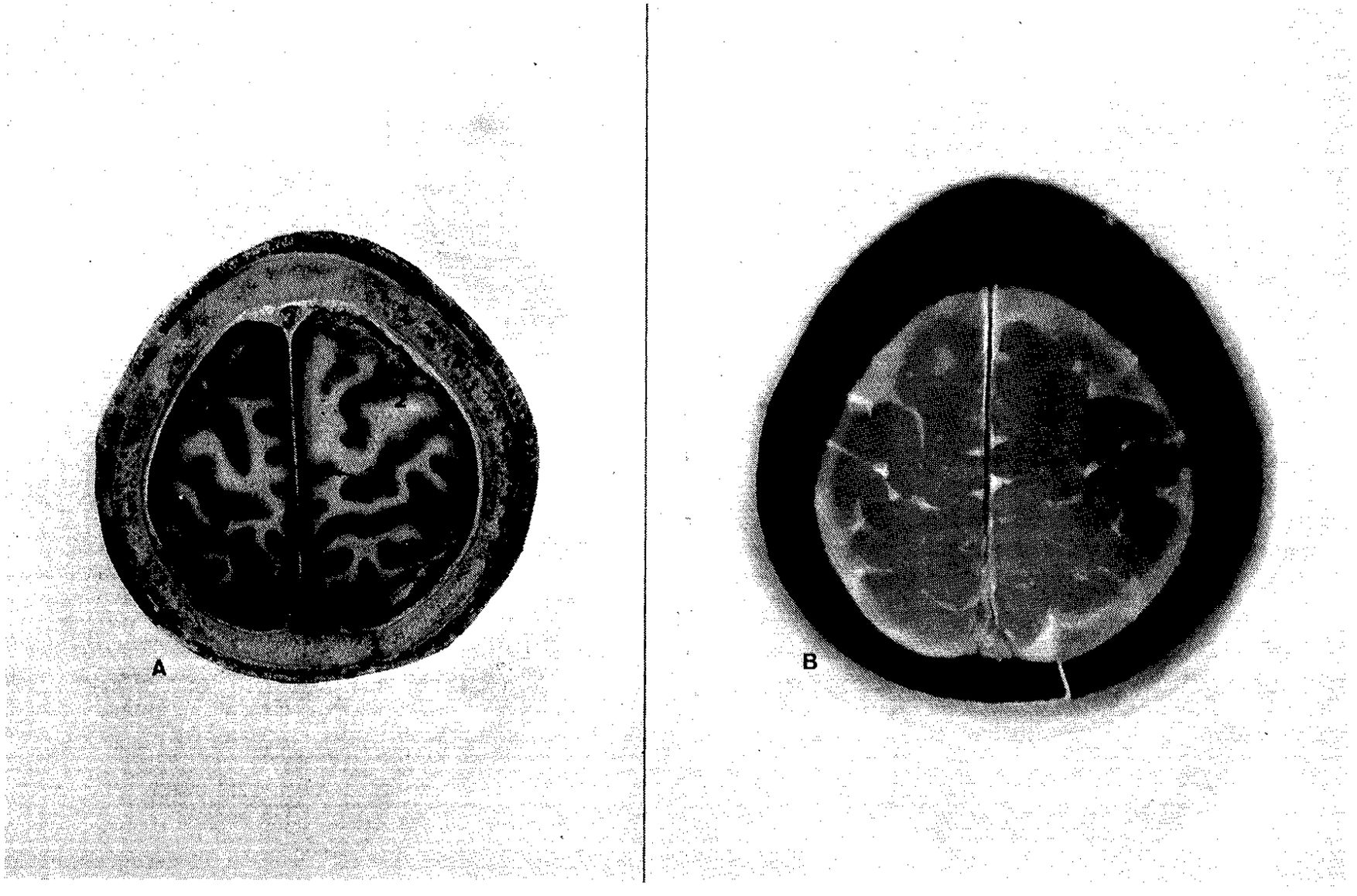

Fig. 13

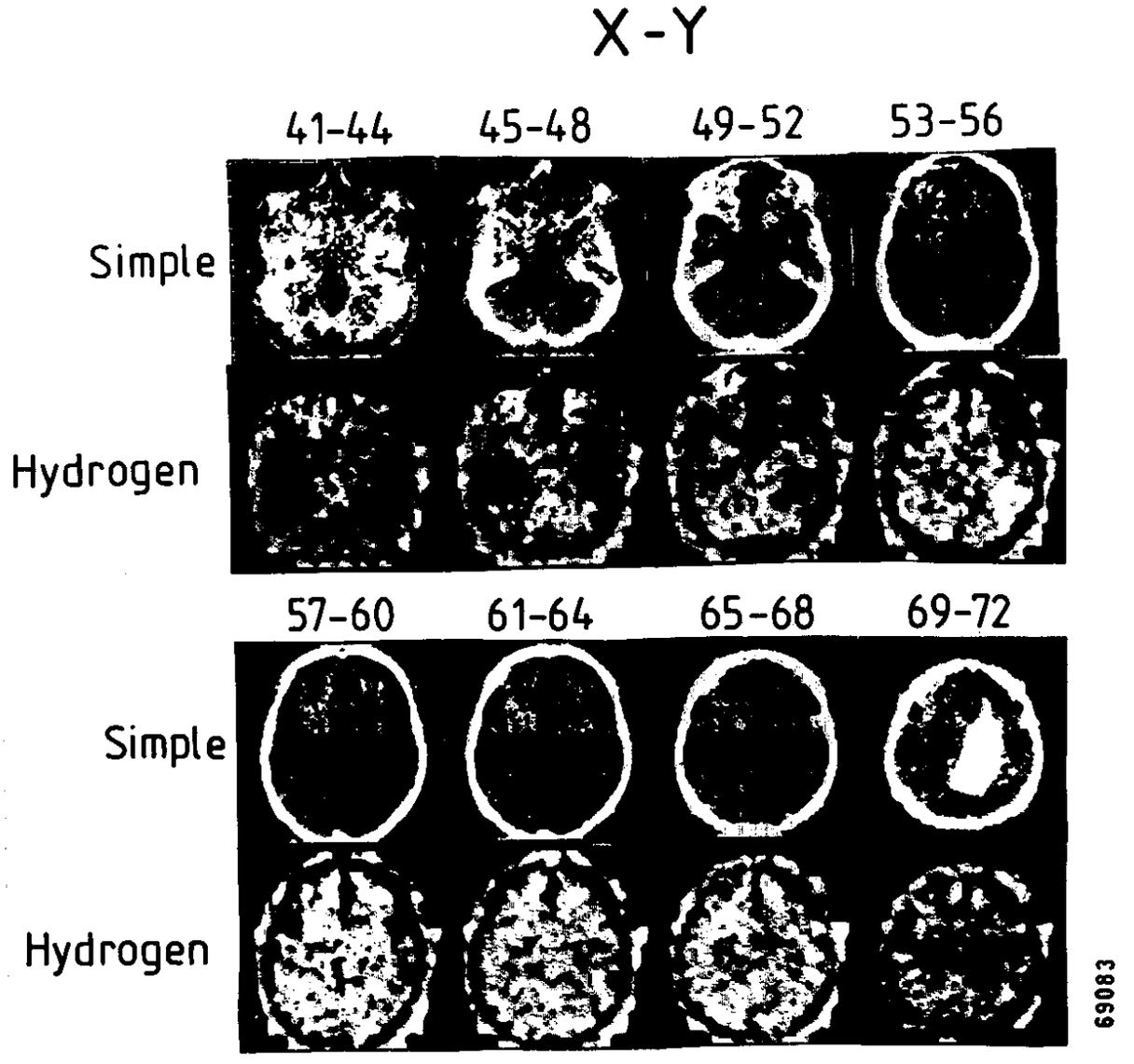
X-Y
41-44
45-48
49-52
53-56
Simple
Hydrogen
57-60
61-64
65-68
69-72
Simple
Hydrogen
69083

Fig. 14

XY SLICE 69-72

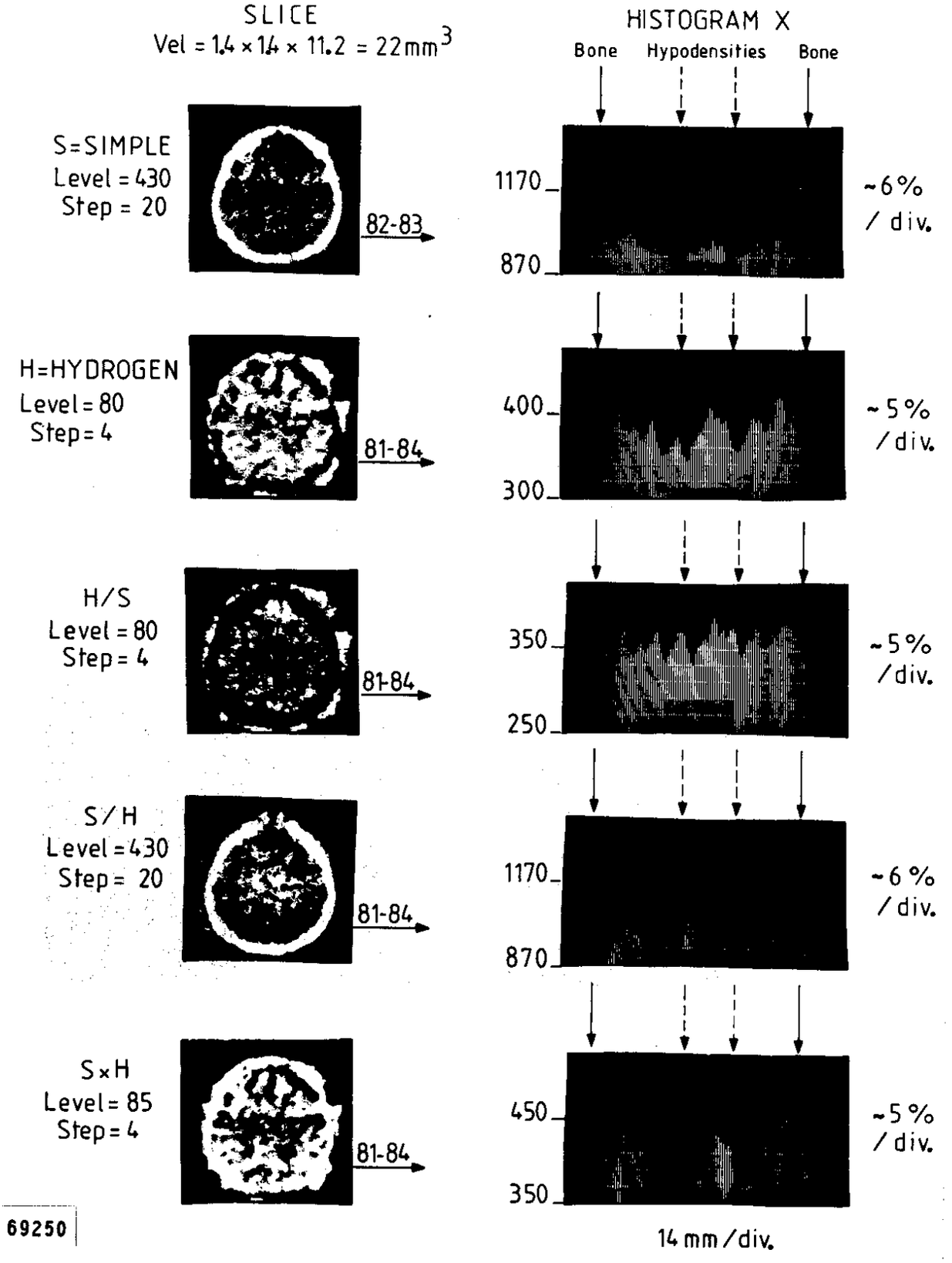

69250

Fig. 15

XY - SIMPLE

PIXEL: 1.4 × 1.4 mm^2

VEL: 5.5 mm^3

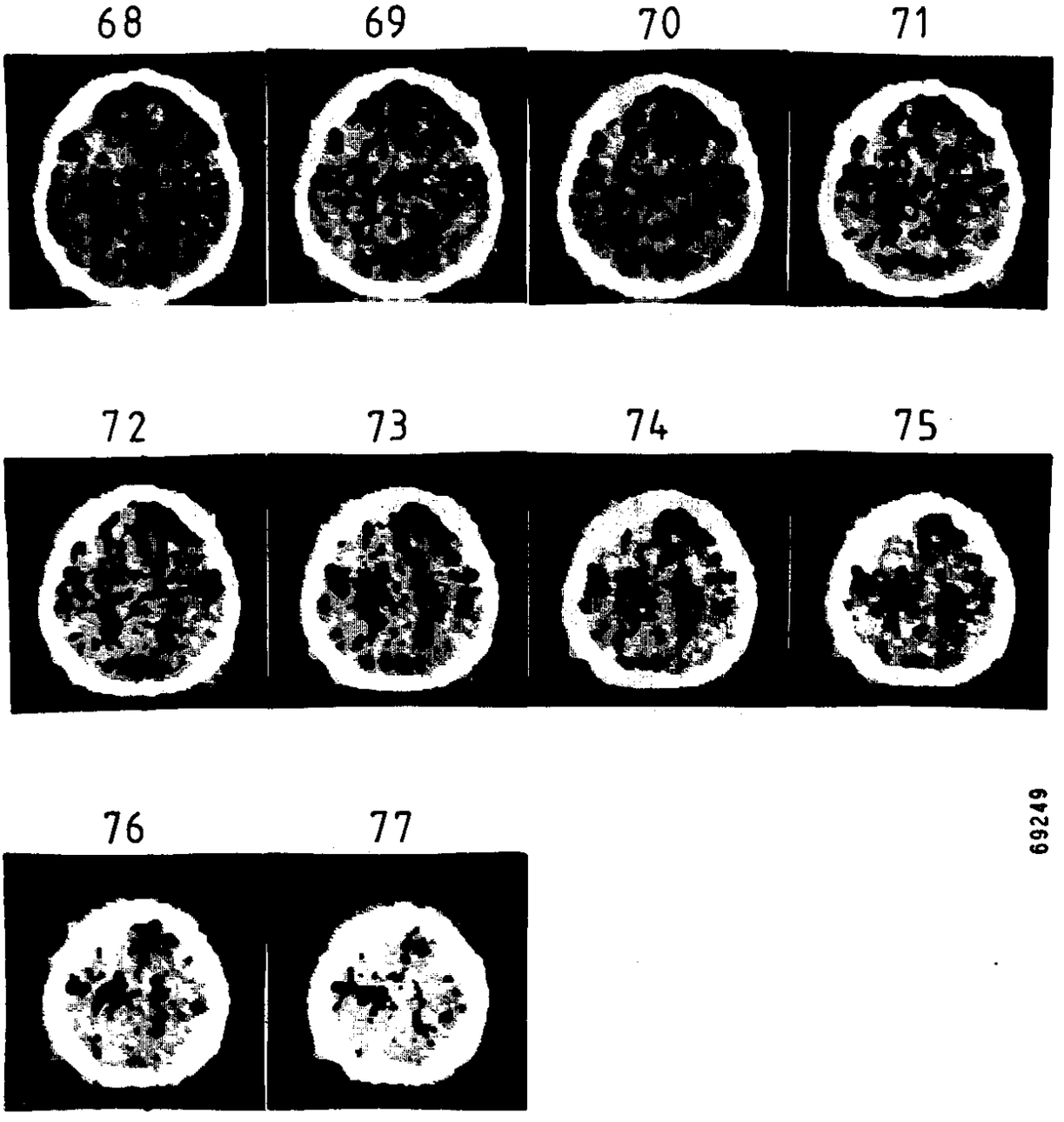

69249

Fig. 16

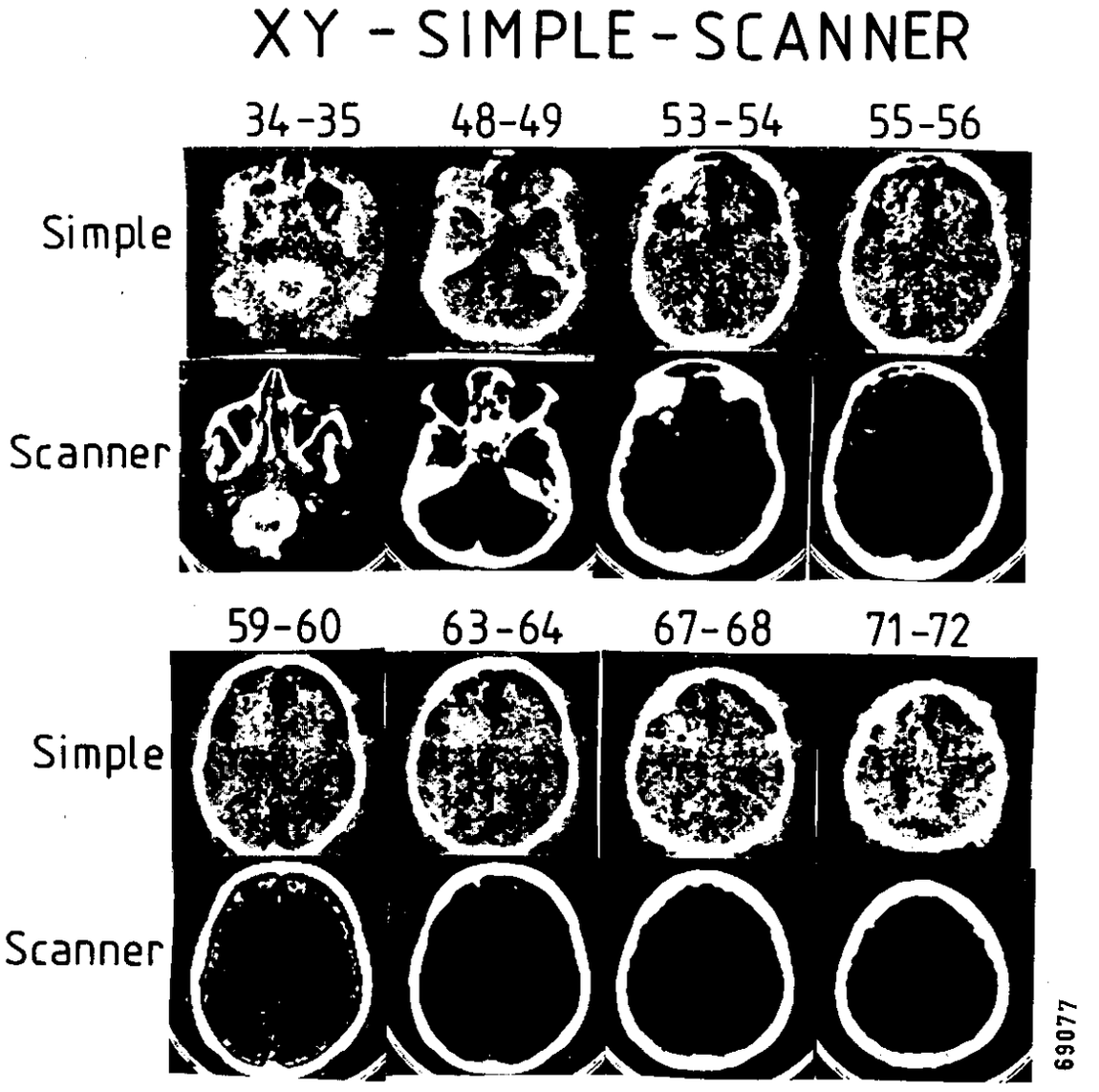
XY - SIMPLE - SCANNER
34-35
48-49
53-54
55-56
Simple
Scanner
59-60
63-64
67-68
71-72
Simple
Scanner
69077

Fig. 17